

Research Article

Mechanical Performance Study of Tower Crane Braced Frame Joint with Different Embedded Part Parameters

Yao Gang,^{1,2} Yang Yang^{1,2} Liao Gang,^{1,2} Huang Zulin,^{1,2} and Weng Bangzheng³

¹Key Laboratory of New Technology for Construction of Cities in Mountain Area, Ministry of Education, Chongqing, China

²School of Civil Engineering, Chongqing University, Chongqing, China

³China Construction Second Engineering Bureau Ltd., Beijing, China

Correspondence should be addressed to Yang Yang; yy20052710@163.com

Received 15 December 2018; Revised 7 June 2019; Accepted 11 June 2019; Published 30 July 2019

Academic Editor: Georgios I. Giannopoulos

Copyright © 2019 Yao Gang et al. This is an open access article distributed under the Creative Commons Attribution License, which permits unrestricted use, distribution, and reproduction in any medium, provided the original work is properly cited.

Embedded part has significant effects on the mechanical performance of tower crane braced frame joint. In this study, a series of experiments with different embedded part parameters are conducted on ultimate bearing capacity, load-displacement relationship, load-strain relationship, failure mode, and failure mechanism. Finite element models are established by the ABAQUS software and compared with the experiment results to verify rationality and credibility of the models. The present experimental study and finite element model analysis focus on the effects of anchor length, anchor width, and endplate area. The research results show that embedded part is pulled out of braced frame joint without plastic deformation, and local stress distribution of braced frame joint is complex with tension, bending, and shear load. The braced frame joint is severely strained and cracked with ultimate bearing capacity. Influence of embedded part parameters on mechanical performance of braced frame joint decreases in the order of anchor length, endplate area, and anchor width. The embedded part parameters have no influence on failure mode but affect the failure mechanism. Ultimate bearing capacity of embedded part is about four times the cracking bearing capacity, and an effective approach to improve ultimate bearing capacity is increasing anchor length. The research results can provide a better understanding of the sensitivity of mechanical and cracking behaviors of tower crane braced frame joint with different embedded part parameters.

1. Introduction

Tower crane safety affects many factors including worker safety, equipment and buildings in the surrounding, and facilities near the construction site even beyond the boundary of the construction site. Many works have been devoted to learning the safety factors of tower crane, the dynamic characteristics and dynamic response of tower crane with external excitation, selection and location of tower crane, and layout planning and management of tower crane. Tower crane safety study outcomes contribute to the knowledge base on tower crane related hazards [1–6]. Appropriate models and control criteria for different cranes are recommended by dynamic analysis, with considering the nonlinear system and multi-degree-of-freedom flexible systems [7–11]. With the aid of computer, the external

excitation and building-crane interaction are considered in the dynamic behavior analysis and application of tower crane. It is found that the effects of seismic wave dimensions and directions, geometric nonlinearity, and the seismic and wind intensities affect the response of a tower crane [12–20].

In previous research by the authors, it is found that embedded part has significant effects on the mechanical performance of tower crane braced frame joint [20, 21]. The tower crane braced frame joint sustains compound stress effect of the tension, flexural, and shear, showing a complex local stress distribution. Possible damage patterns of the embedded parts include the cross-sectional area of the tensile strength of anchor plate, weld connection, overall punching damage considering the group anchorage effect, and bending damage of narrow limbs outside the wall. However, mechanical performance of braced frame joint

with different embedded part parameters is not clear, and relevant studies are conducted to address the effects.

In this study, a series experiments of with different embedded part parameters are conducted on ultimate bearing capacity, load-displacement relationship, load-strain relationship, failure mode, and failure mechanism. Finite element models are established by the ABAQUS software and compared with the experiment results to verify rationality and credibility of the models. Braced frame joint specimens with four different embedded part parameters are prepared. In the experiments, the effects of embedded part parameters of braced frame joint specimens on the mechanical and cracking behaviors are first investigated. Then, five different anchor lengths of embedded part parameters in braced frame joint specimens are tested to study the influence of anchor length on mechanical performance. At last, five different endplate areas of embedded part parameters in braced frame joint specimens are tested to study the influence of endplate area on mechanical performance.

The pressure sensor (CZLYB-481) and rebound strain gage (YCW-100AA) are adopted to obtain the complete displacement-load curves of embedded part parameters. The static strain chamber (DH3816N) and digital strain gage (SDY-2202) are adopted to obtain the complete stress-strain curves of braced frame joint specimens. Simultaneously, the crack width observer (HC-CK101) is used to measure the crack width. Digital single lens reflex (DSLR) is used to record crack initiation and ultimate failure.

This paper is organized as follows: the experimental setup is described in Section 2 in detail. The effects of the embedded part parameters on mechanical and cracking behaviors in braced frame joint specimens are studied in Section 3. Material model, damage model, and information of finite element model are given in Section 4. The influence of embedded part parameters on mechanical and cracking behaviors in braced frame joint specimens is investigated in Section 4. Conclusions are drawn in Section 5.

2. Experimental Setup

2.1. Specimen Preparation. To investigate the sensitivity of mechanical performance of embedded part parameter to braced frame joint, parallelepiped specimens with four different embedded part parameters are prepared for pullout test. In construction stage, standard section of tower crane connects with the frame beam through high-strength bolts, and frame beam is then connected with the shear wall through the embedded parts; the most commonly used tower crane braced frame joint is shown in Figure 1.

Scale model experiments with a 1/2 reduced-scale of embedded part are adopted in this paper considering the maximum tension stress in the test equipment. Karp [22] exposes standard plane formulation of dynamic response of material orthotropic and frequency of excitation. Clayton et al. [23] and Wei et al. [24] also prove that external load effect only influences stress field distribution within a certain range by composite structure experiments. The best location of measuring devices based on well-known static data for composite structure according to Saint-Venant's principle is

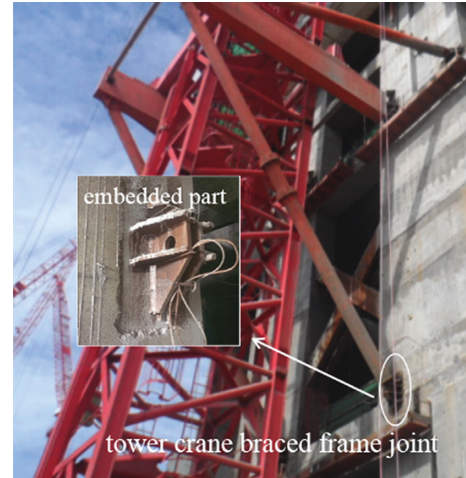


FIGURE 1: Tower crane braced frame joint in construction stage.

recommended twofold size of research area with appropriate boundary conditions. In view of economy and test rationality, the braced frame joint specimen size could be increased in threefold with the embedded part. The material is consistent with the actual engineering, and the concrete grade is C30. The embedded part is made of Q345C steel plate, and the nominal yield strength is 345.0 MPa. The dimensions of tested braced frame joint specimens are approximately 1000.0 mm in length, 600.0 mm in width, and 300.0 mm in thickness, as shown in Figure 2.

The embedded part parameter, to a great extent, controls the mechanical performance of braced frame joint. Embedded part is composed of five parts, including ear plate, stiffening plate, face plate, anchor, and endplate. Embedded part is an axisymmetric structure, and four of the anchors and endplates have the same parameters, respectively. Displacement and extreme stress in key locations of embedded part can reflect mechanical performance to a certain extent. Therefore, two strain gages are placed in bottom middle of anchor 1 and anchor 4 and named strain gage U and strain gage D, respectively. Four schemes of embedded part parameters are designed for the preparation of specimens, as shown in Table 1. The embedded part with different parameters is repeatable. External force is mainly undertaken by anchors of embedded part, and hence anchor width (W), anchor length (H), endplate length (A), and endplate width are taken as variables to research the mechanical performance of embedded part.

2.2. Testing System. The test is completed in the structural laboratory of Chongqing University. Braced frame joints are subjected to a monotonically axial loading by a hydraulic jack device, as shown in Figure 3. Considering limitations of test site and loading instrument, the test device is designed by the principle of leverage. Steel beam A is placed on the top of testing system to provide drawing force. The loading actuator protrudes from the middle hole of the steel beam A. During loading process, hydraulic jack transmits the thrust to the steel beam A. Due to the leverage, intermediate

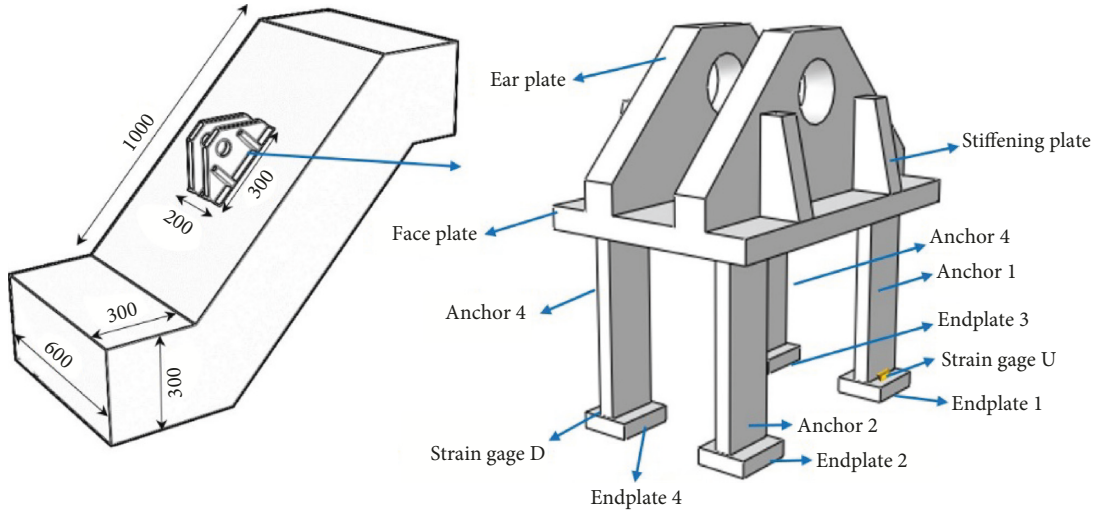


FIGURE 2: Dimension of tested braced frame joint specimen and embedded part (mm).

TABLE 1: Four schemes of embedded part parameters (mm).

Scheme	Anchor width (W)	Anchor length (H)	Endplate length (A)	Endplate width
W50-A55-H1	50	160	55	45
W50-A55-H2	50	200	55	45
W50-A70-H1	50	160	70	65
W40-A55-H1	40	160	55	45

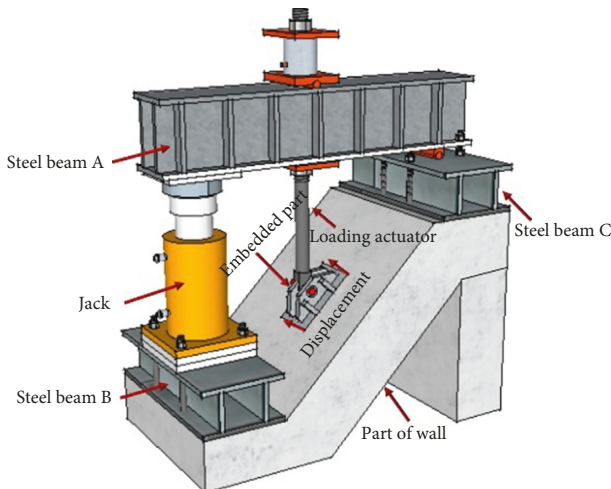


FIGURE 3: Digital control system of testing devices.

tension rod bears twice the thrust of the hydraulic jack, and finally the drawing force is added to the embedded part through the loading actuator. Steel beams B and C are used to fix the specimen. The steel beam is provided with stiffeners to improve the rigidity of the steel beam and reduce the deformation of the steel beam. The loading rate is controlled at a loading speed of 1.0 mm/min. At this slow loading rate, the initiation, propagation, and coalescence processes of cracks within specimens can be clearly observed. The axial load and axial strain values can be acquired continuously by a data acquisition system with the maximum rate of 100 data points per second. The test device and instrument system are

fully digital, which are capable and flexible to operate displacement-controlled loading.

The test devices and instruments include a hydraulic jack, pressure sensor, static digital strain gage, static strain chamber, strain gage, and crack width observer. Detailed parameters are shown in Table 2, and location of displacement measurement and strain stage is given in Figure 4. Laser calibration is used in the installation process of testing devices, and the laser calibration provides both the veracity and the reproducibility of the displacement and strain analysis.

3. Analysis of Experimental Results

3.1. Loading Process Characteristics. The crack initiation mode plays an important role in the ultimate failure mode under uniaxial tension [25, 26]. Thus, it is necessary to study the process of crack initiation modes in the specimens under uniaxial tension. In the present experiment, the applied loads, strain of embedded part, displacement of embedded part, and the specimen deformations are simultaneously recorded by the testing system. To study the effect of embedded part parameters on the mechanical performance of the braced frame joint specimens under uniaxial tension, the complete load-displacement curves of embedded part containing characteristic values are plotted together in Figures 5–8. Load characteristic value states and ultimate failure states captured by the DSLR are also inserted in Figures 5–8.

The load-displacement curves in Figure 5 can be divided into three stages, cracking stage, the crack extension stage,

TABLE 2: Main parameters of test device and instrument.

Devices	Specification	Resolution	Range	Measurement object
Digital strain gage	SDY-2202	$1 \mu\epsilon$	$1 \pm 19999 \mu\epsilon$	Load
Pressure sensor	CZLYB-481	0.1 kN	150 kN	Load
Rebound strain gage	YCW-100AA	≤ 0.01 mm	100 mm	Displacement
Static strain chamber	DH3816N	$0.01 \mu\epsilon$	$1 \pm 19999 \mu\epsilon$	Strain
Crack width observer	HC-CK101	≤ 0.02 mm	40 mm	Crack width

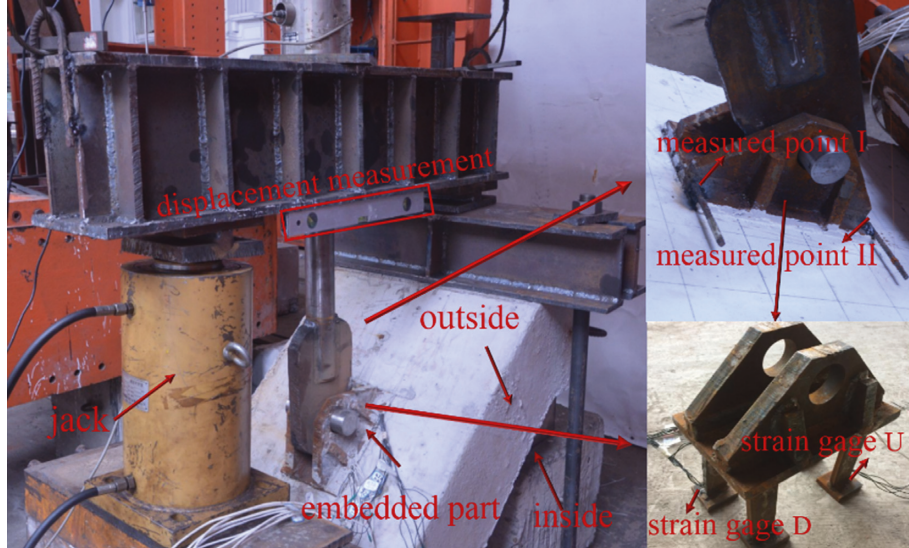


FIGURE 4: Location of displacement measurement and strain stage.

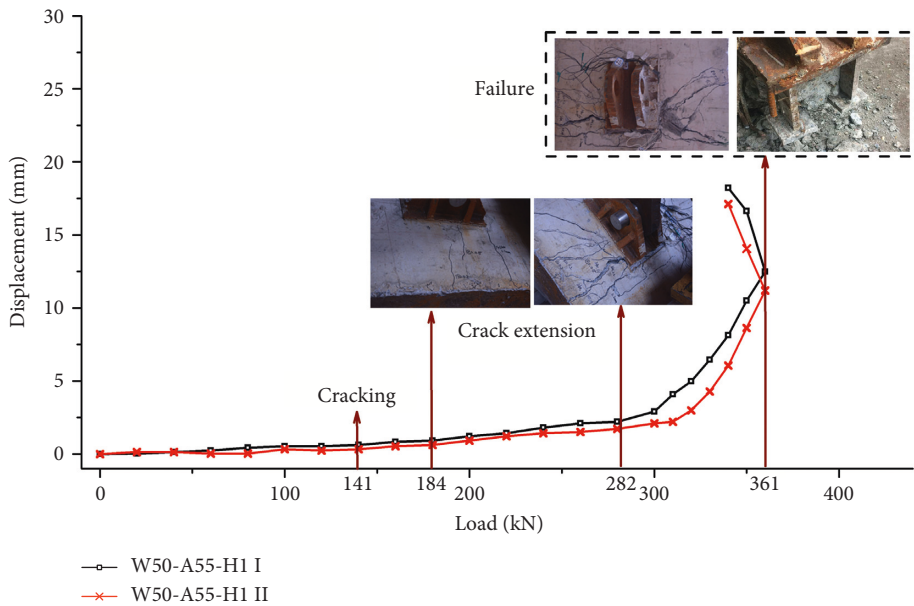


FIGURE 5: Fully load-displacement curves of W50-A55-H1 specimen.

and failure stage. Load at first crack is 141.0 kN, and the first tensile crack at the bottom of embedded part penetrates specimen surface with a 2.6 mm crack. Two tensile cracks appear when the load is increased to 184.0 kN; one of the tensile cracks is 2.0 mm in width and the other is 1.6 mm in width. Mixed tensile-shear cracks appear along the bottom

of embedded part which penetrate specimen surface with the increasing of load. Shear cracks appear at bottom center of embedded part when the load is increased to 282.0 kN, with a 2.2 mm width. Concrete at bottom center of embedded part is displacement damaged with lateral uplift. When load is increased 361.0 kN, the upper corner of the embedded part

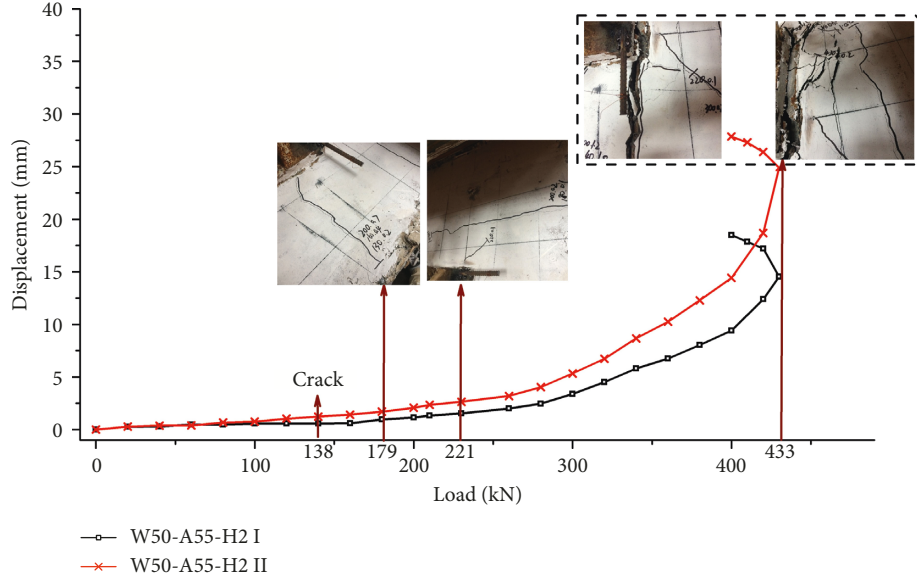


FIGURE 6: Fully load-displacement curves of W50-A55-H2 specimen.

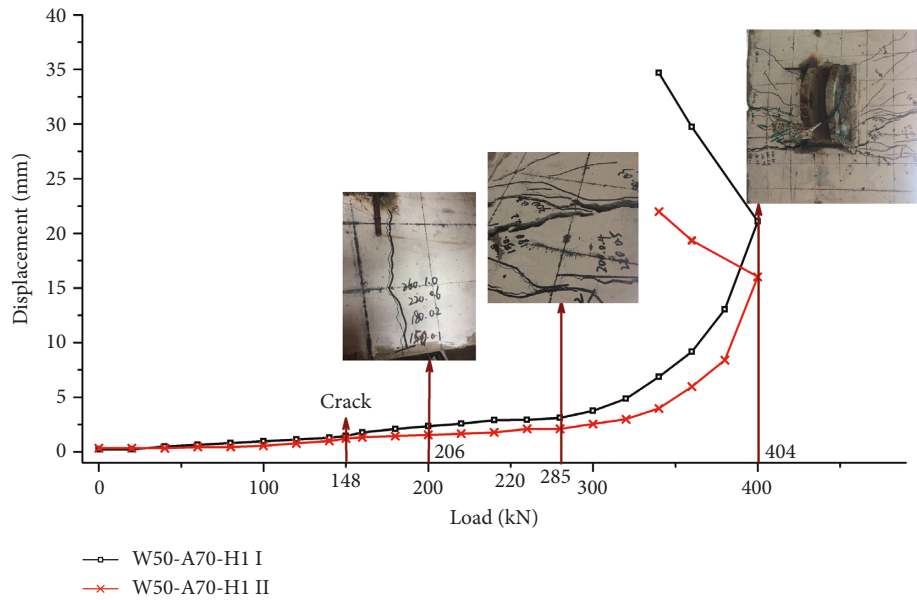


FIGURE 7: Fully load-displacement curves of W50-A70-H1 specimen.

produced an oblique crack in the direction of 45° with 2.4 mm width. The length of the crack on the side of the specimen exceeded one-half of the height of the section, and the specimen is broken along the main crack with the 361.0 kN load. The lower side of the embedded part that bonded to the concrete reaches the ultimate tensile strength and is damaged. In the postpeak regime, the progressive load drops take place, which is associated with the progressive failure of specimens. When the specimen is finally destroyed, there are two main tensile cracks with 10.8 mm and 11.2 mm, and the largest main shear crack was 10.6 mm.

From the load-displacement curves in Figure 6, it can be seen that cracking load is 138.0 kN. The first tensile crack at the bottom of embedded part penetrates with a 2.2 mm crack

across the specimen surface. When the load reaches 179.0 kN, a shear crack appears across the specimen surface at a 20.0 cm distance, with a 2.0 mm width. At the underside corner of embedded part, a similar mixed tensile-shear crack initiation mode occurs with an angle of approximately 45° . The crack initiation mode varies from the tensile crack initiation mode to the shear crack initiation mode with the increasing load. The first tensile crack penetrates the section, and the width increases when the loading is 221.0 kN. Mixed tensile-shear cracks occur at the top corner of embedded part with an angle of approximately 45° when the load reaches 360.0 kN. The ultimate load is 433.0 kN, the embedded part is pulled out, and the outside of the specimen is crushed. Concrete at the right bottom of embedded part is

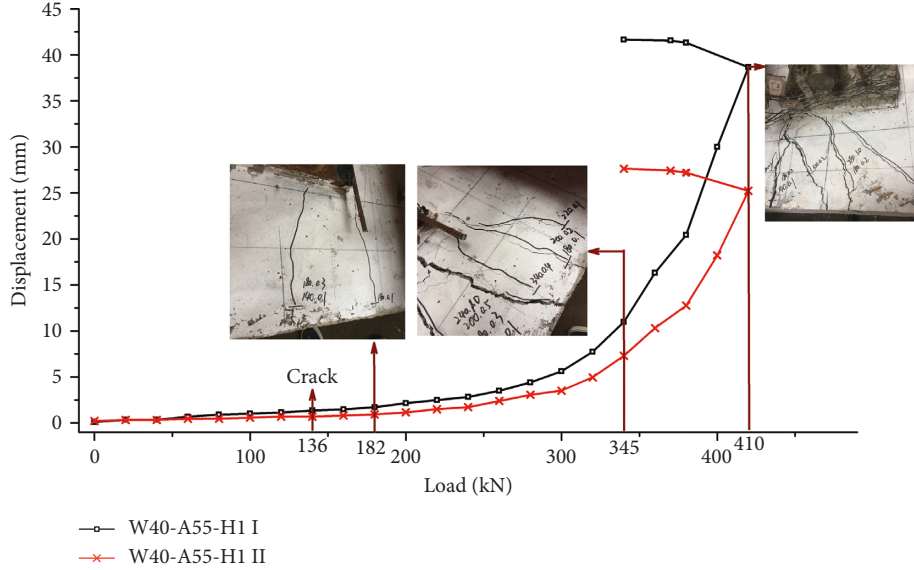


FIGURE 8: Fully load-displacement curves of W40-A55-H1 specimen.

damaged. The displacement of up embedded part reaches 14.5 mm, and displacement of bottom embedded part reaches 24.8 mm with a clockwise rotation.

From the load-displacement curves in Figure 7, it can be seen that cracking load increases to 148.0 kN. The first transverse tensile crack occurs at the bottom of embedded part with a 1.6 mm width when the load reaches 206.0 kN. Crack occurs at the specimen side simultaneously with a length more than 75.0 mm. More and more mixed tensile-shear cracks appear with the increasing load, and the mixed tensile-shear cracks appear at the top corner of embedded part when the load increases to 285.0 kN. Number and width of tensile cracks and mixed tensile-shear cracks grow with the increase of load. The W50-A70-H1 specimen is in an ultimate failure state when the load is 404.0 kN. The displacement of top embedded part reaches 13.2 mm, and displacement of bottom embedded part reaches 21.1 mm with a clockwise rotation.

From the load-displacement curves in Figure 8, it can be seen that cracking load is 136.0 kN, and small cracks occur at the bottom side of embedded part. The first mixed tensile-shear cracks appear at the middle of embedded part with a load of 182.0 kN. More and more mixed tensile-shear cracks appear with the increasing of load, and the mixed tensile-shear cracks appear at the top corner of embedded part when the load increases to 345.0 kN. Number and width of tensile cracks and mixed tensile-shear cracks grow with the increase of load. The W40-A55-H1 specimen is in an ultimate failure state when the load is 410.0 kN. The displacement of top embedded part reaches 12.1 mm, and displacement of bottom embedded part reaches 19.1 mm with a clockwise rotation. The average ratios of the crack initiation stress to the peak stress in the four specimens under uniaxial are 0.389, 0.302, 0.375, and 0.341 respectively. It can be observed that the average ratio of crack initiation stress to peak stress decreases as the embedded part parameters increase. This phenomenon is related to the crack initiation mode in the four specimens subjected to uniaxial tension.

3.2. Stress-Strain Characteristics. The quantitative evidence on the displacement and strain of embedded part in specimens can be obtained using digital strain gage techniques. Fully load-strain curves of four specimens are shown in Figure 9, and the locations of strain are also given.

Load-strain curves of four specimens have small difference before the cracking load, and distinction becomes obvious after the cracking load. All of the strains drop down after the embedded parts are pulled out. This finding supports the notion that embedded part of deformation is elastic deformation, and it is not destroyed. The W50-A55-H1 specimen has larger strain in both strain gage D and strain gage U than the W50-A55-H2 specimen, and this phenomenon could be attributable to the effect of anchor length. W50-A55-H1 specimen strains change faster than W50-A55-H2 specimen strains. This finding supports the notion that anchor length affects the concrete volume which participates in resisting the tensile force. The W40-A55-H2 specimen has the largest strain in both strain gage D and strain gage U, and the W50-A70-H1 specimen has the smallest strain in both strain gage D and strain gage U. This phenomenon could be attributable to the effect of anchor width and endplate area.

Anchor length is the biggest factor for affecting the mechanical performance in three embedded part parameters. The cracks of specimens with different anchor lengths have larger differences than others, and the final failure modes of specimens are given in Figure 10.

Cracks of specimens can be distributed into three classes, tensile crack, tensile-shear crack, and shear crack. Cracks of the W50-A55-H1 specimen concentrate mainly on central and bottom of embedded part. However, cracks of the W50-A55-H2 specimen concentrate mainly on bottom of embedded part. The W50-A55-H1 specimen has more tensile-shear cracks than the W50-A55-H2 specimen. Simultaneously, location of last tensile crack of the W50-A55-H2 specimen is lower than the W50-A55-H1 specimen.

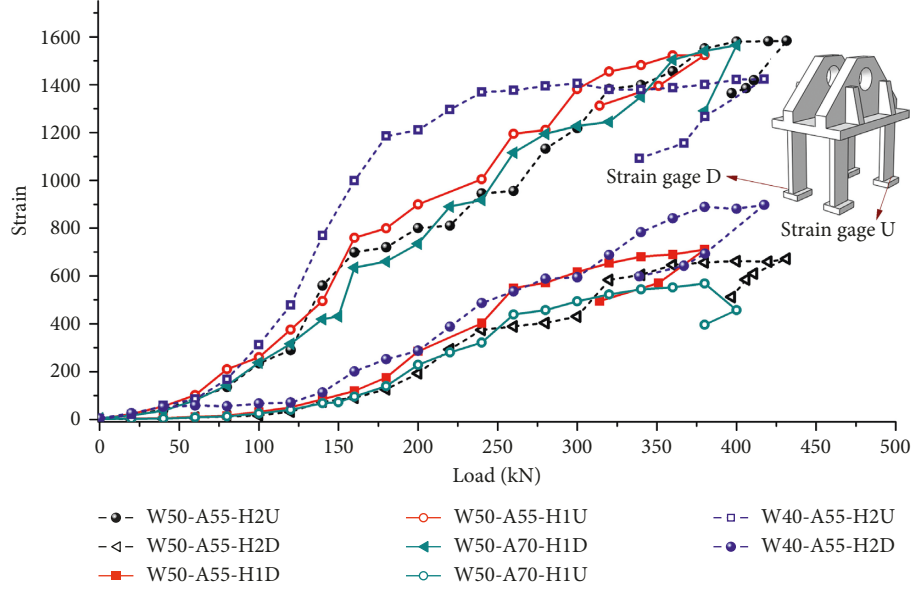


FIGURE 9: Fully load-strain curves of four specimens.

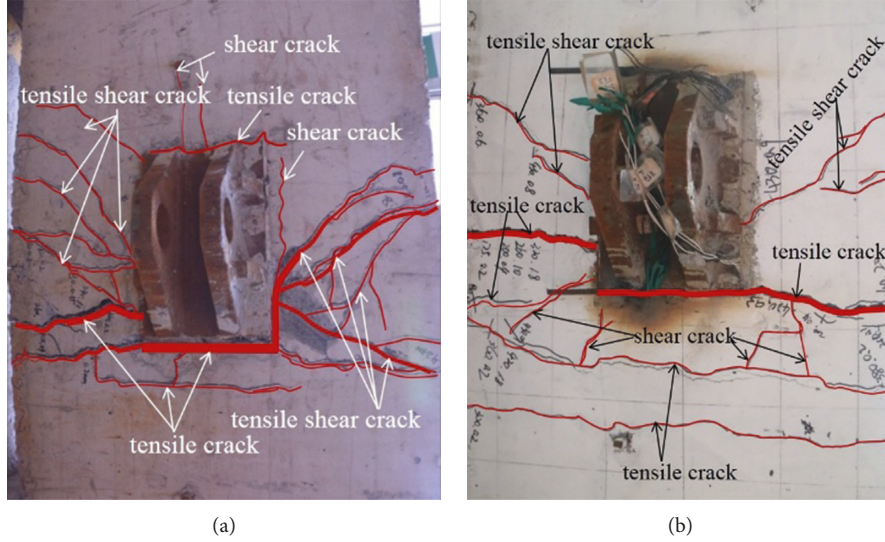


FIGURE 10: Failure modes of specimens. (a) W50-A55-H1. (b) W50-A55-H2.

Moreover, it can be found from Figure 10 that tensile-shear crack concentrates mainly on 45° angle. In addition, it can also be observed from Figure 10 that the tension can be divided into normal tension and tangential stress. The reason of bending moment is that there is a distance between tangential stress and specimen.

The main tensile crack at the bottom of embedded part is the effect of bending moment. It can be concluded from Figure 10 that the number of tensile-shear crack decreases with the increase of the anchor length.

4. Finite Element Model and Damage Model

4.1. Material Models. In the finite element analysis, the materials are all based on the nonlinear elastic constitutive

model and are defined by the material property parameters. Nonlinear analysis is considered in the model according to nonlinear elastic constitutive model of materials. The stress-strain equations of concrete under uniaxial compression are as follows:

$$\sigma_c = (1 - d_c) E_c \varepsilon, \quad (1)$$

$$d_c = \begin{cases} 1 - \frac{f_{c,r} n}{E_c \varepsilon_{c,r} (n - 1 + (\varepsilon / \varepsilon_{c,r})^n)}, & \frac{\varepsilon}{\varepsilon_{c,r}} \leq 1, \\ 1 - \frac{f_{c,r}}{E_c \varepsilon_{c,r} \alpha_c ((\varepsilon / \varepsilon_{c,r}) - 1)^2 + E_c \varepsilon_{c,r} (\varepsilon / \varepsilon_{c,r})}, & \frac{\varepsilon}{\varepsilon_{c,r}} \geq 1, \end{cases} \quad (2)$$

$$n = \frac{E_c \varepsilon_{c,r}}{E_c \varepsilon_{c,r} - f_{c,r}}. \quad (3)$$

The stress-strain equations of concrete under uniaxial tensile are as follows:

$$\sigma_t = (1 - d_t) E_c \varepsilon, \quad (4)$$

$$d_t = \begin{cases} 1 - \frac{f_{t,r}}{E_c \varepsilon_{t,r}} \left[1.2 - 0.2 \left(\frac{\varepsilon}{\varepsilon_{t,r}} \right)^5 \right], & \frac{\varepsilon}{\varepsilon_{t,r}} \leq 1, \\ 1 - \frac{\rho_t}{\alpha_t (\varepsilon / \varepsilon_{t,r} - 1)^{1.7} + \varepsilon / \varepsilon_{t,r}}, & \frac{\varepsilon}{\varepsilon_{t,r}} \geq 1, \end{cases} \quad (5)$$

where α_t and α_c are descending stage parameters in uniaxial tension stress-strain and uniaxial compression stress-strain, respectively, $f_{t,r}$ and $f_{t,c}$ are representative values of uniaxial tensile and compressive strength of concrete, respectively, $\varepsilon_{t,r}$ and $\varepsilon_{c,r}$ are tension strain and compression strain, respectively, d_t and d_c are tension damage parameter and compression damage parameter, respectively, and E_c is elastic modulus of concrete. Double slant constitutive model is taken in rebar and embedded part and given in the following equation:

$$\sigma_s = \begin{cases} f_y + 0.01(\varepsilon_s - \varepsilon_y)E_s, & \varepsilon_y \leq \varepsilon_s \leq \varepsilon_u, \\ E_s \varepsilon_s, & \varepsilon_s \leq \varepsilon_y, \end{cases} \quad (6)$$

where f_y is yield stress, ε_s is strain of steel, E_s is elastic modulus of steel, and ε_y and ε_u are yield strain and ultimate strain, respectively.

4.2. Damage Model. The plastic damage constitutive model in ABAQUS can simulate the tensile cracking and compressive crushing of concrete materials, considering the isotropic elastic damage and plastic behavior of materials. Hence, the plastic damage constitutive model has been considered in this paper. Tensile and compressive damage constitutive relationship is given in Figure 11. Tensile and compressive damage factor can be defined from the following equations:

$$D_t = 1 - \frac{\sigma_t E_0^{-1}}{\varepsilon_t^{\text{pl}} \left(1 / \left(\varepsilon_t^{\text{pl}} / \varepsilon_t^{\text{in}} - 1 \right) \right) + \sigma_t E_0^{-1}}, \quad (7)$$

$$D_c = 1 - \frac{\sigma_c E_0^{-1}}{\varepsilon_c^{\text{pl}} \left(1 / \left(\varepsilon_c^{\text{pl}} / \varepsilon_c^{\text{in}} - 1 \right) \right) + \sigma_c E_0^{-1}}, \quad (8)$$

where $\varepsilon_c^{\text{pl}}$ and $\varepsilon_t^{\text{pl}}$ are compressive plastic strain and tensile plastic strain, respectively, $\varepsilon_c^{\text{in}}$ is inelastic strain and $\varepsilon_t^{\text{in}}$ is cracking strain, and σ_c and σ_t are compression and tension, respectively.

Three-dimensional numerical models are established to study the mechanical performance of braced frame joint. In order to improve the computational efficiency, half models are taken to simplify the finite element model in axis-symmetry specimen. According to parameters of the specimen, the same material properties, section size,

reinforcement ratio, and boundary conditions are given in Tables 3 and 4.

Integral model is comprised of rebar, embedded part, and concrete component, which are independent parts. Hence, the interaction needs to be defined by a certain contact relation. The definition of the contact between embedded part and concrete is essential to ensure the accuracy of the simulation. The loads, boundary conditions, and load conditions are defined using the load function module of ABAQUS. The embedded part element is embedded in the concrete element with “Embedded Region” command in ABAQUS. The “surface to surface contact” of ABAQUS is used to solve the contact problem between the surfaces of embedded part and concrete component. The deformation coordination of concrete elements is realized by setting the contact property of friction. The Coulomb friction model is used and the friction coefficient is assumed to be 0.3. A particular mesh refinement in concrete component is given around embedded part, where stresses concentrate and damage propagates. Details of finite element models are given in Figure 12.

To investigate the effects of the anchor length on the fracturing behaviors in the braced frame joint specimens under uniaxial tension, the specimens with different anchor lengths are analyzed using finite element model. The corresponding displacement, stress, and damage factors (D_t and D_c) are calculated by finite element model. In this paper, the anchor length varies from 120.0 mm to 200.0 mm at an identical interval of 20.0 mm; fully load-displacement curves of specimens on the location of displacement measurement II are shown in Figure 13. Figure 14–16 show the ultimate failure patterns of braced frame joint specimens containing different anchor lengths under uniaxial tension.

It can be found from Figure 13 that the numerical simulation results of load-displacement curves with 160 mm and 200 mm anchor lengths are in good agreement with measured specimens in testing. The deviation of measured simulation results with 160 mm and 200 mm anchor lengths is 2.76% and 4.13% respectively, and both of them are less than 5.00%. Thus, it can be concluded that the finite element models in this part are quite accurate and credible. It can also be observed from Figure 13 that the development of braced frame joint specimens is almost same in the process of destruction including elastic stage, crack stage, and failure stage. Moreover, the loading of three stages increases with the increase of anchor length. Ultimate bearing capacity of braced frame joint increases with the increase of the anchor length. When the anchor length varies from 120.0 mm to 200.0 mm at an identical interval of 20.0 mm, the ultimate bearing capacities are 301.70 kN, 323.32 kN, 350.08 kN, 359.32 kN, and 427.66 kN, respectively. Ultimate bearing capacity is improved 41.75% when the anchor length is enlarged 66.67%.

It can be found from Figure 14 that the stress concentrations occur near the crack trajectories in the specimens at the ultimate failure state. Simultaneously, the following can be observed from process of calculation: anchor length has an evident effect on cracking load and the developing speed

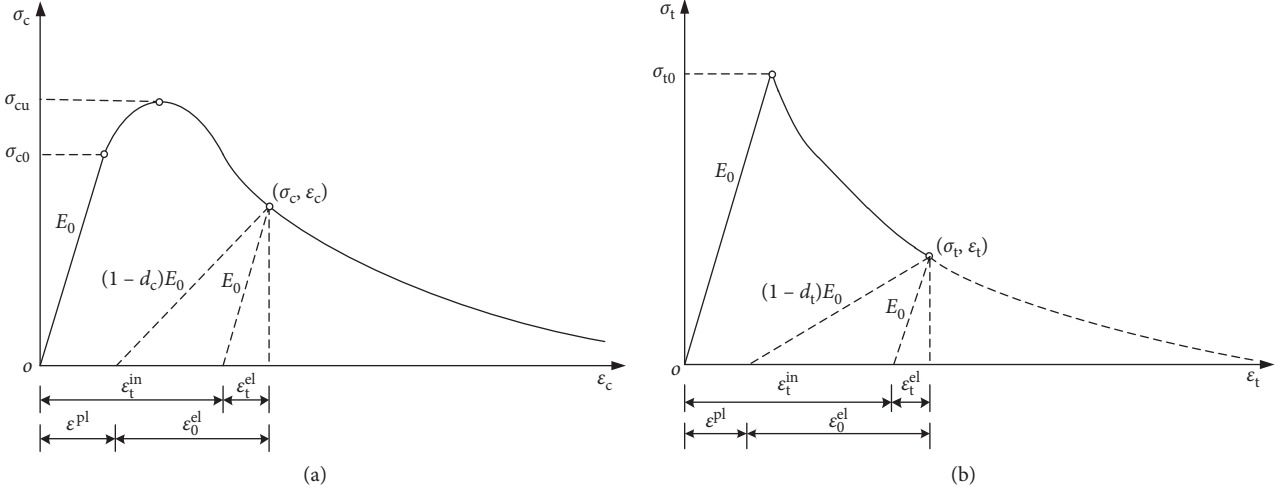


FIGURE 11: Uniaxial damage constitutive curve of concrete compression. (a) Uniaxial tension. (b) Uniaxial compression.

TABLE 3: Steel material properties in finite element model.

Description	Material	Yield stress	Ultimate strength	Poisson ratio	Elastic modulus	Element selection
Embedded part	Q345 B steel	379.07 MPa	550.7 MPa	0.3	2.08×10^5 MPa	C3D8R
Rebar	$\phi 8$ HRB400	426.1 MPa	567.6 MPa	0.25	2.07×10^5 MPa	T3D2
Rebar	$\phi 10$ HRB400	433.3 MPa	583.3 MPa	0.3	2.11×10^5 MPa	T3D2

TABLE 4: Concrete material properties in finite element model.

Description	Material	Compressive strength	Tensile strength	Elastic modulus	Element selection
Concrete component	C20 concrete	17.6 MPa	1.76 MPa	2.55×10^4 MPa	C3D8R
Concrete component	C30 concrete	21.09 MPa	2.09 MPa	3.03×10^4 MPa	C3D8R
Concrete component	C40 concrete	33.6 MPa	3.36 MPa	3.25×10^4 MPa	C3D8R
Concrete component	C50 concrete	40.0 MPa	4.00 MPa	3.45×10^4 MPa	C3D8R
Concrete component	C60 concrete	48.0 MPa	4.80 MPa	3.60×10^4 MPa	C3D8R

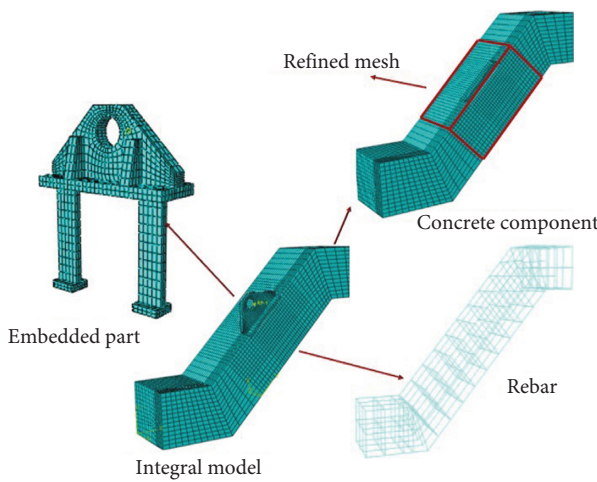


FIGURE 12: Finite element model of braced frame joint.

of crack. Cracking load of braced frame joint increases with the increasing of the anchor length; meanwhile, the developing speed of crack decreases with the increase of the

anchor length. At the early stage of loading, displacement of embedded parts increases slowly with the increase of loading, and the specimens are in linear elastic stage. At the cracking stage of loading, displacement of embedded parts increases rapidly with the increase of loading; meanwhile, the rigidity degeneration is obvious, and it is mainly between crack and yield. Specimens show obvious nonlinear characteristic and certain ductility in this process. It can be found from Figure 14 that the stress of embedded part is in the range of emergency capacity. Stress distributes uniformly when the anchor length increases. It can be found from Figures 15 and 16 that damaged areas of braced frame joint specimens extend from the center to both ends with the increase of anchor length. The damaged area develops along the height direction. Cracking of brace frame joint is more comprehensive, and energy dissipation capacity is stronger. The percentages of damage volumes and damagec volumes in the region of 0.8 to 0.99 are taken to analyze quantitatively. The percentages of damage volumes are 22.6%, 25.9%, 32.1%, 38.7%, and 47.9%, respectively, when anchor lengths are 120 mm, 140 mm, 160 mm, 180 mm, and 200 mm. The percentages of damagec volumes are 12.1%,

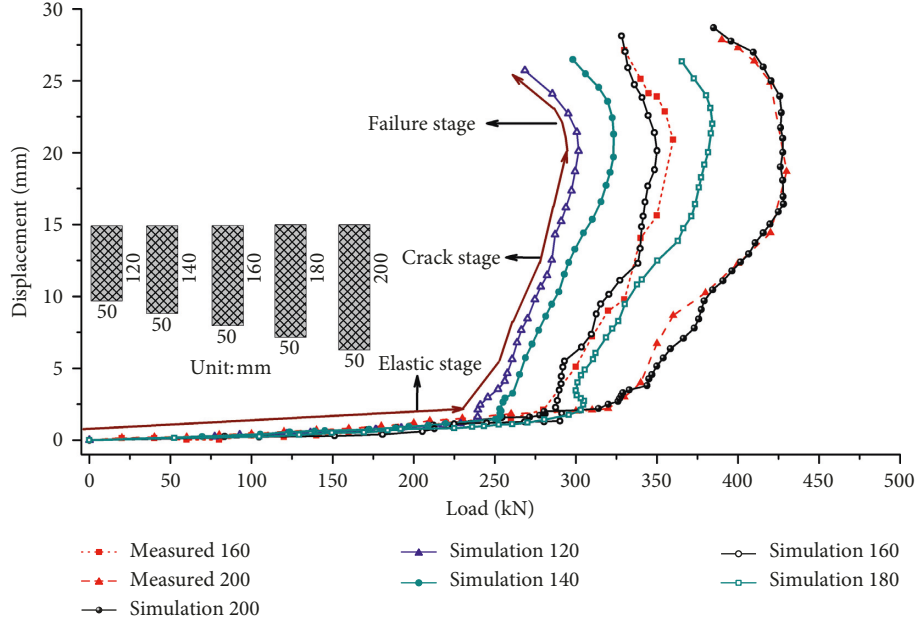


FIGURE 13: Fully load-displacement curves of specimens with different anchor lengths.

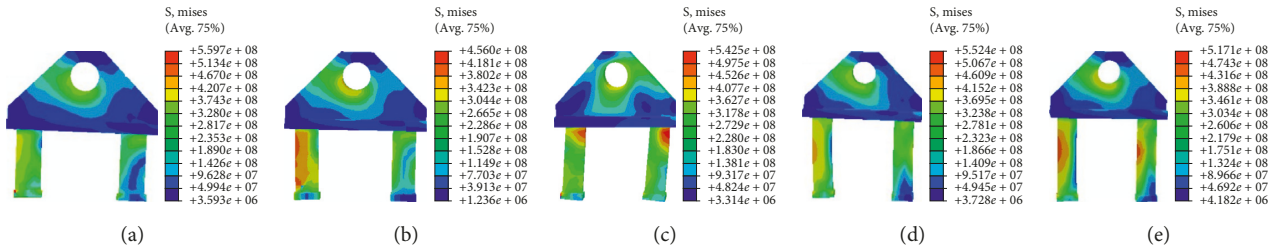


FIGURE 14: Embedded part numerical stress distribution with different anchor lengths (MPa). (a) 120 mm. (b) 140 mm. (c) 160 mm. (d) 180 mm. (e) 200 mm.

15.7%, 19.1%, 23.6%, and 32.5%, respectively, when anchor lengths are 120 mm, 140 mm, 160 mm, 180 mm, and 200 mm. The anchor length of embedded part affects the concrete volumes of resisting tension. Concrete volumes of resisting tension increase with the increase of anchor length. The failure reason of braced frame joint specimen is the limitation of concrete tensile strength.

4.3. Endplate Areas. Increasing the endplate area of anchor is convenient in engineering practice, and at the same time, this operation seems to contribute to the bearing capacity of the specimen from the above tests. Consequently, it is necessary to investigate the effects of the endplate area on the fracturing behaviors in the braced frame joint specimens under uniaxial tension, and the specimens with different endplate areas are analyzed using finite element model. The corresponding displacement, stress, and damage factors (D_t and D_c) are calculated by the finite element model. In this paper, the endplate area varies from 2000.0 mm^2 to 4200.0 mm^2 at an identical edge length interval of 5.0 mm; fully load-displacement curves of

specimens on the location of displacement measurement II are shown in Figure 17. Figures 18–20 show the ultimate failure patterns of braced frame joint specimens containing different endplate areas under uniaxial tension.

It can be found from Figure 17 that the numerical simulation results of load-displacement curves with 2475.0 mm^2 and 4200.0 mm^2 endplate area are in good agreement with measured specimens in testing. Thus, it can be concluded that the finite element models in this part are quite accurate and credible. It can also be observed from Figure 17 that the development of braced frame joint specimens is almost same in the process of destruction including elastic stage, crack stage, and failure stage. Moreover, the loading of three stages increases with the increase of endplate area. Ultimate bearing capacity of braced frame joint increases with the increase of the endplate area. When the endplate area varies from 2000.0 mm^2 to 4200.0 mm^2 at an identical edge length interval of 5.0 mm, the ultimate bearing capacities are 337.81 kN, 350.08 kN, 373.57 kN, 386.68 kN, and 389.59 kN, respectively. Ultimate bearing capacity changes more obvious when the endplate area is less than 3000.0 mm^2 ; meanwhile, the ultimate

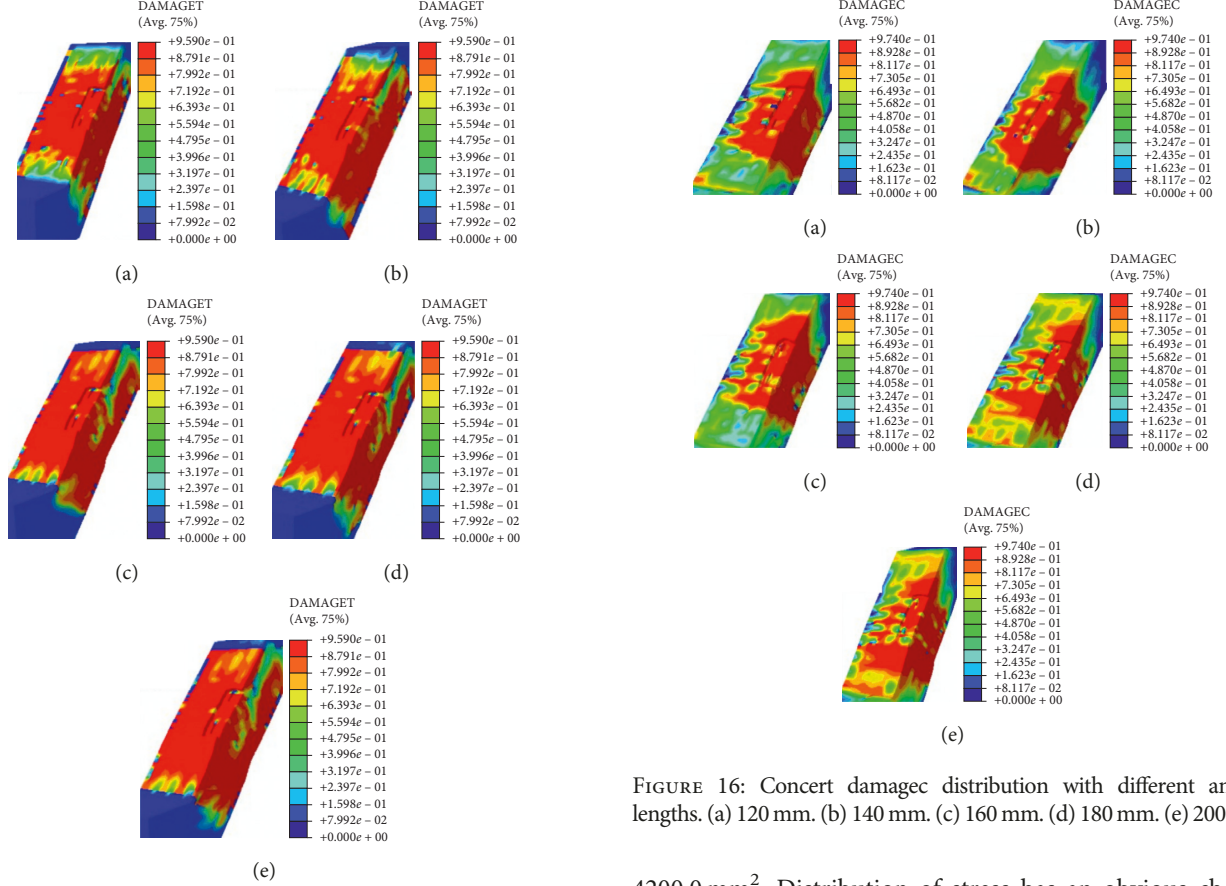


FIGURE 15: Concert damaget distribution with different anchor lengths. (a) 120 mm. (b) 140 mm. (c) 160 mm. (d) 180 mm. (e) 200 mm.

bearing capacity maintains stability when endplate area is more than 3000.0 mm^2 . It can be concluded that the tension can be simplified as transverse shear and vertical tension along specimen surfaces. Vertical tension along specimen surfaces becomes the control load for the reason that concrete has a low tensile strength. Consolidation force of concrete increases with the enlarging of endplate area at first; thus, the ultimate bearing capacity increases with the increase of endplate area. It can be concluded that the consolidation force in the endplate is the control load. However, the ultimate bearing capacity maintains stability at later stage. It can be speculated that control load changes from consolidation force in the endplate to concrete tensile strength. Specimens with different endplate area show more comparability than specimens with different anchor length. Specimens with different endplate area show similar characteristics at the early stage of loading and cracking stage of loading. Endplate area has a certain effect on the fracturing behaviors in the braced frame joint specimens, and the effect mitigates when the endplate area reaches a certain value.

It can be found from Figure 18 that the stress of embedded part is in the range of emergency capacity. The extreme stress is in junction of front panel and anchor when the endplate area is 2000.0 mm^2 . The stress concentrations occur near the left anchor of embedded part in the specimen at the ultimate failure state when the endplate area is

FIGURE 16: Concert damagec distribution with different anchor lengths. (a) 120 mm. (b) 140 mm. (c) 160 mm. (d) 180 mm. (e) 200 mm.

4200.0 mm^2 . Distribution of stress has an obvious change with the increase of endplate area when the endplate area enlarges from 2000.0 mm^2 to 2475.0 mm^2 . Distribution of stress has a small change when the endplate area goes on increasing. It can be found from Figures 19 and 20 that damaget of braced frame joint specimens has nearly no change with the increase of endplate area; meanwhile, damagec of braced frame joint specimens has an obvious change. The percentages of damaget volumes and damagec volumes in the region of 0.8 to 0.99 are taken to analyze quantitatively. The percentages of damaget volumes are 32.1%, 32.6%, 32.9%, 33.7%, and 33.9%, respectively, when endplate areas are 2000 mm^2 , 2475 mm^2 , 3000 mm^2 , 3575 mm^2 , and 4200 mm^2 . The percentages of damagec volumes are 19.1%, 16.7%, 14.3%, 11.6%, and 9.5%, respectively, when endplate areas are 2000 mm^2 , 2475 mm^2 , 3000 mm^2 , 3575 mm^2 , and 4200 mm^2 . Concretes at the surrounding of endplates are crushed, and the embedded part has a slippage when the endplate area is 2000.0 mm^2 . With the increase of endplate area, the vertical tension along the specimen surface has reached the concrete tensile strength before the concretes at the surrounding of endplates are crushed. Based on the above analysis, the failure modes follow the same principle in these five specimens, but there is a different interaction between embedded part and concrete.

5. Conclusions

In this study, a series of experiments with different embedded part parameters are conducted on ultimate bearing

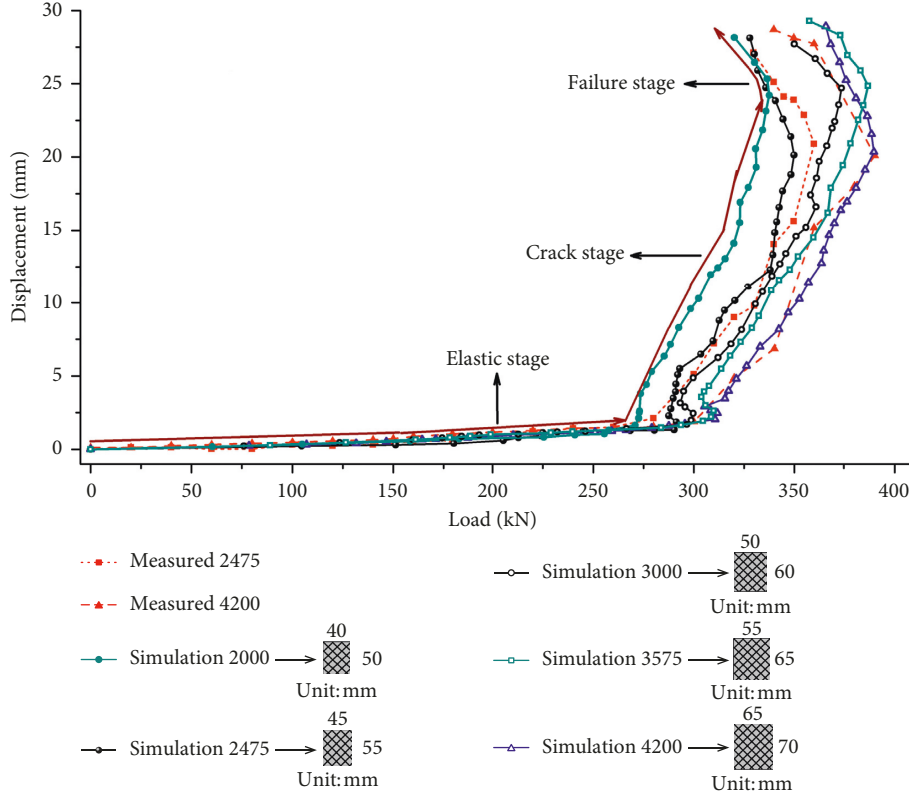


FIGURE 17: Fully load-displacement curves of specimens with different endplate areas.

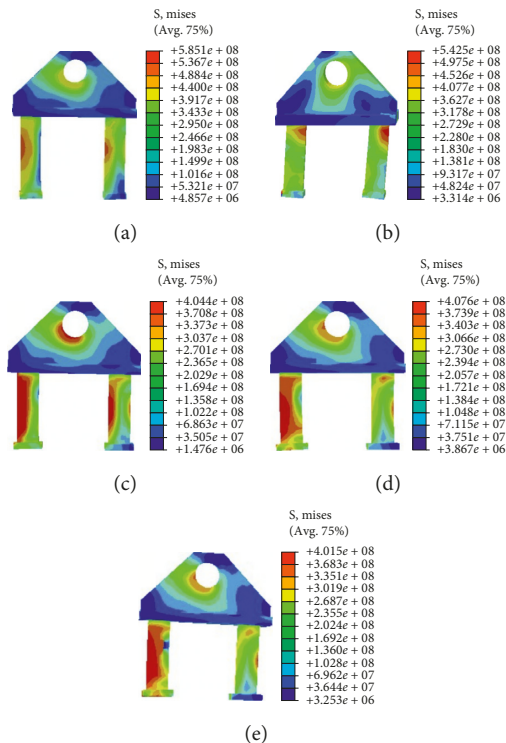


FIGURE 18: Embedded part numerical stress distribution with different endplate areas (mm^2). (a) 2000 mm^2 . (b) 2475 mm^2 . (c) 3000 mm^2 . (d) 3575 mm^2 . (e) 4200 mm^2 .

capacity, load-displacement relationship, load-strain relationship, failure modes, and failure mechanism. Finite element models are established by software and compared with the experiment results to verify rationality and credibility of the models. The present experimental study and finite element model analysis focus on the effects of anchor length, anchor width, and endplate area. The research conclusions are as follows:

- (1) Embedded part is pulled out of tower crane braced frame joint without plastic deformation, and local stress distribution of tower crane braced frame joint is complex with tension, bending, and shear load. The braced frame joint is severely strained and cracked with ultimate bearing capacity. Influence of embedded part parameters on mechanical performance of tower crane braced frame joint decreases in the order of anchor length, endplate area, and anchor width.
- (2) Ultimate bearing capacity of embedded part is about four times the cracking load, and an effective approach of improving ultimate bearing capacity is increasing anchor length. Average ratio of crack initiation stress to peak stress decreases as the embedded part parameters increase.
- (3) Cracks of specimens can be distributed into three classes, tensile crack, tensile-shear crack, and shear crack. The main tensile crack at the bottom of

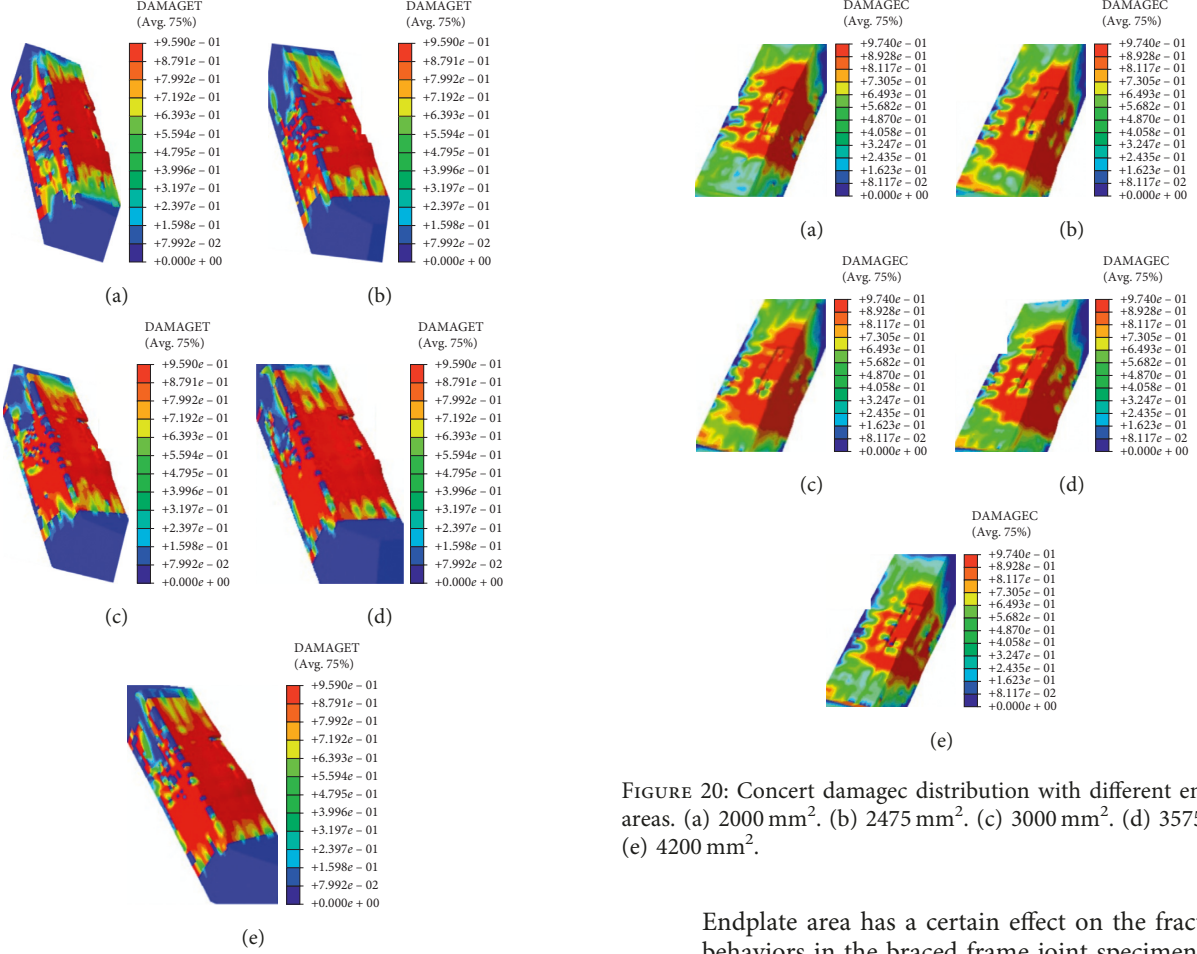


FIGURE 19: Concert damaget distribution with different endplate areas. (a) 2000 mm^2 . (b) 2475 mm^2 . (c) 3000 mm^2 . (d) 3575 mm^2 . (e) 4200 mm^2 .

embedded part is the effect of bending moment. The cracks of specimens with different anchor lengths have larger differences than other embedded part parameters.

- (4) The development of braced frame joint specimens is almost same in the process of destruction including elastic stage, crack stage, and failure stage. Stress concentrations occur near the crack trajectories in the specimens at the ultimate failure state. The stress of embedded part is in the range of emergency capacity. The anchor length of embedded part affects the concrete volume of resisting tension. Concrete volume of resisting tension increases with the increase of anchor length. The failure reason of braced frame joint specimen is the limitation of concrete tensile strength.
- (5) Ultimate bearing capacity changes more obvious when the endplate area is small; meanwhile, the ultimate bearing capacity maintains stability when endplate area reaches a certain value. Specimens with different endplate area show more comparability than specimens with different anchor lengths.

FIGURE 20: Concert damagec distribution with different endplate areas. (a) 2000 mm^2 . (b) 2475 mm^2 . (c) 3000 mm^2 . (d) 3575 mm^2 . (e) 4200 mm^2 .

Endplate area has a certain effect on the fracturing behaviors in the braced frame joint specimens, and the effect mitigates when the endplate area reaches a certain value. The failure modes follow the same principle with different endplate areas, but there is a different interaction between embedded part and concrete.

Data Availability

The data used to support the findings of this study are available from the corresponding author upon request.

Conflicts of Interest

The authors declare no conflicts of interest.

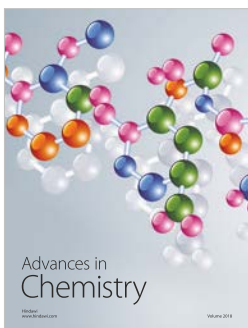
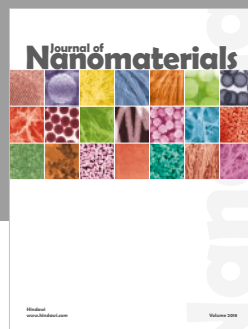
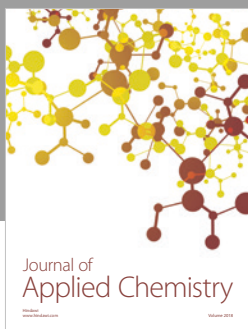
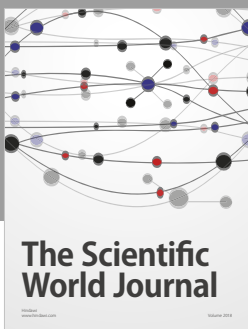
Acknowledgments

This work was supported by the Fundamental Research Funds for Central Universities (2019CDQYTM028, 2019CDXYTM0032, and 106112017CDJXY200009) and National Natural Science Foundation of China (51608074).

References

- [1] W. Zhou, T. Zhao, W. Liu, and J. Tang, “Tower crane safety on construction sites: a complex sociotechnical system perspective,” *Safety Science*, vol. 109, pp. 95–108, 2018.

- [2] A. Shapira and B. Lyachin, "Identification and analysis of factors affecting safety on construction sites with tower cranes," *Journal of Construction Engineering and Management*, vol. 135, no. 1, pp. 24–33, 2009.
- [3] G. Raviv, B. Fishbain, and A. Shapira, "Analyzing risk factors in crane-related near-miss and accident reports," *Safety Science*, vol. 91, pp. 192–205, 2017.
- [4] V. W. Y. Tam and I. W. H. Fung, "Tower crane safety in the construction industry: a Hong Kong study," *Safety Science*, vol. 49, no. 2, pp. 208–215, 2011.
- [5] R. Xie, T. M. Tian, and Q. Tian, "Damage causes of tower cranes during Wenchuan earthquake in Xi'an city," *Crgoes Handling Machines*, vol. 4, pp. 1–3, 2009.
- [6] I. J. Shin, "Factors that affect safety of tower crane installation/dismantling in construction industry," *Safety Science*, vol. 72, pp. 379–390, 2015.
- [7] E. M. Abdel-Rahman, A. H. Nayfeh, and Z. N. Masoud, "Dynamics and control of cranes: a review," *Modal Analysis*, vol. 9, no. 7, pp. 863–908, 2003.
- [8] J. Feng and S. C. Yoo, "Dynamic analysis of tower cranes," *Journal of Engineering Mechanics*, vol. 131, no. 1, pp. 88–96, 2005.
- [9] Hazriq Izzuan Jaafar, Z. Mohamed, J. J. Jamian, A. F. Z. Abidin, A. M. Kassim, and Z. Ab Ghani, "Dynamic behaviour of a nonlinear gantry crane system," *Procedia Technology*, vol. 11, pp. 419–425, 2013.
- [10] Y. Şahin, M. Levent, and K. Hira, "Analysis of active vibration control of multi-degree-of-freedom flexible systems by Newmark method," *Simulation Modelling Practice and Theory*, vol. 69, pp. 136–148, 2016.
- [11] S. C. Wang, R. S. Shen, T. H. Jin, and S. J. Song, "Dynamic behavior analysis and its application in tower crane structure damage identification," *Advanced Materials Research*, vol. 368–373, pp. 2478–2482, 2012.
- [12] B. Ai, J. L. Yang, and Z. Z. Pei, "Seismic response analysis of tower crane in consideration of the building-crane interaction," *Applied Mechanics and Materials*, vol. 353–356, pp. 1981–1985, 2013.
- [13] H. Li-Jeng and S. Hong-Jie, "Seismic response analysis of tower crane using SAP2000," *Procedia Engineering*, vol. 79, pp. 513–522, 2014.
- [14] Y. H. He, L. C. Gu, and P. B. Ji, "Seismic analysis of tower crane based on ANSYS," *Machinery Design and Manufacture*, vol. 7, pp. 188–190, 2012.
- [15] Y. L. Li, B. Ai, and B. Li, "The damage cause of tower crane under earthquake action and the status of dynamic analysis," *Special Structures*, vol. 28, no. 2, pp. 66–68, 2011.
- [16] T. Shen, W. M. Yan, D. X. Zhou, C. Li, and K. Hao, "TMD control and analysis of cranes under earthquake," *Technology for Earthquake Disaster Prevention*, vol. 12, no. 2, pp. 276–287, 2017.
- [17] Abuduwalisi, R. F. Yu, and Y. X. Yu, "Spatial variation of ground motions based on Wenchuan acceleration records," *Journal of Vibration and Shock*, vol. 32, no. 16, pp. 70–75, 2013, in Chinese.
- [18] T. G. Mara, "Effects of a construction tower crane on the wind loading of a high-rise building," *Journal of Structural Engineering*, vol. 136, no. 11, pp. 1453–1460, 2010.
- [19] X. D. Wei, X. H. Wu, J. Qian et al., "Research on nonlinear time-history response of a multi-tower connected structure subjected to vertical earthquake motion," *Building Structure*, vol. 42, no. 6, pp. 121–126, 2012.
- [20] G. Yao, H. Li, Y. Yang et al., "Seismic responses and dynamic characteristics of boom tower crane basing on measured strong earthquake excitation," *Journal of Vibroengineering*, vol. 21, no. 1, pp. 154–169, 2019.
- [21] G. Yao, C. Xu, Y. Yang, M. Wang, M. Zhang, and A. Thabeet, "Working mechanism of a high-performance tower crane attached to wall joints," *Journal of Engineering Science and Technology Review*, vol. 11, no. 1, pp. 19–27, 2018.
- [22] B. Karp, "Dynamic end effects in an orthotropic strip," *International Journal of Solids and Structures*, vol. 125, pp. 43–49, 2017.
- [23] P. M. Clayton, J. W. Berman, and L. N. Lowes, "Subassembly testing and modeling of self-centering steel plate shear walls," *Engineering Structures*, vol. 56, pp. 1848–1857, 2013.
- [24] M.-W. Wei, J. Y. Richard Liew, D. Yong, and X.-Y. Fu, "Experimental and numerical investigation of novel partially connected steel plate shear walls," *Journal of Constructional Steel Research*, vol. 132, pp. 1–15, 2017.
- [25] Y. Fu, X. Zhou, and M. Kou, "An improved coupled thermomechanic bond-based peridynamic model for cracking behaviors in brittle solids subjected to thermal shocks," *European Journal of Mechanics—A/Solids*, vol. 73, pp. 282–305, 2019.
- [26] Y. Wang, X. Zhou, and X. Xu, "Numerical simulation of propagation and coalescence of flaws in rock materials under compressive loads using the extended non-ordinary state-based peridynamics," *Engineering Fracture Mechanics*, vol. 163, pp. 248–273, 2016.



Hindawi

Submit your manuscripts at
www.hindawi.com

